Article:
Howard, F.H.N., Al-Janabi, H., Patel, P. et al. (2022) Nanobugs as drugs: bacterial derived nanomagnets enhance tumor targeting and oncolytic activity of HSV-1 virus. Small, 18 (13). 2104763. ISSN: 1613-6810

https://doi.org/10.1002/smll.202104763

NANO · MICRO small
www.small-journal.com

Nanobugs as Drugs: Bacterial Derived Nanomagnets Enhance Tumor Targeting and Oncolytic Activity of HSV-1 Virus

Faith H N Howard, Haider Al-Janabi, Priya Patel, Katie Cox, Emily Smith, Jayakumar Vadakekolathu, A. Graham Pockley, Joe Conner, James F Nohl, Dan A Allwood, Cristal Collado-Rojas, Aneurin Kennerley, Sarah Staniland, and Munitta Muthana**

The survival strategies of infectious organisms have inspired many therapeutics over the years. Indeed the advent of oncolytic viruses (OVs) exploits the uncontrolled replication of cancer cells for production of their progeny resulting in a cancer-targeting treatment that leaves healthy cells unharmed. Their success against inaccessible tumors however, is highly variable due to inadequate tumor targeting following systemic administration. Coassembling herpes simplex virus (HSV1716) with biocompatible magnetic nanoparticles derived from magnetotactic bacteria enables tumor targeting from circulation with magnetic guidance, protects the virus against neutralizing antibodies and thereby enhances viral replication within tumors. This approach additionally enhances the intratumoral recruitment of activated immune cells, promotes antitumor immunity and immune cell death, thereby inducing tumor shrinkage and increasing survival in a syngeneic mouse model of breast cancer by 50%. Exploiting the properties of such a nanocarrier, rather than tropism of the virus, for active tumor targeting offers an exciting, novel approach for enhancing the bioavailability and treatment efficacy of tumor immunotherapies for disseminated neoplasms.

1. Introduction

Microorganisms possess highly evolved survival strategies which have been exploited to address drug delivery. In oncology the concept of "bugs as drugs" can exploit the direct cytotoxic activity of chemical therapies, while also enabling the development of robust, therapeutic anticancer immunity. For example, oncolytic viruses (OVs) can selectively infect and replicate in cancer cells to result in both direct tumor cell lysis and the induction of immunogenic cell death (ICD) and antitumor immunity. As a result, OVs are an emerging cancer therapeutic modality which is positioned at the interface of biologic therapy and immunotherapy. The application of OVs using viruses, such as herpes simplex virus (HSV), vesicular stomatitis virus (VSV), adenovirus (Ad), and Amgen's T-VEC,[1] the first FDA approved OV for clinical use against melanoma, in

F. H. N. Howard, H. Al-Janabi, P. Patel, K. Cox, C. Collado-Rojas, M. Muthana
Department of Oncology and Metabolism
Mellanby Centre for Bone Research
University of Sheffield
Beech Hill Road, Sheffield S10 2RX, UK
E-mail: f.howard@sheffield.ac.uk; m.muthana@sheffield.ac.uk

E. Smith
NMRC
School of Chemistry
University of Nottingham
Nottingham NG7 2RD, UK

The ORCID identification number(s) for the author(s) of this article can be found under https://doi.org/10.1002/smll.202104763.

DOI: 10.1002/smll.202104763

J. Vadakekolathu, A. G. Pockley
John van Geest Cancer Research Centre
Centre for Health, Ageing and Understanding Disease (CHAUD)
School of Science and Technology
Nottingham Trent University
Nottingham NG11 8NS, UK

J. Conner
Invizius Ltd
BioCity, Bo'ness road, Newhouse ML1 5UH, UK

J. F. Nohl, D. A. Allwood
Department of Materials Science and Engineering
University of Sheffield
Mappin Street, Sheffield S1 3JD, UK

A. Kennerley
Department of Chemistry
University of York
Heslington, York YO10 5DD, UK

S. Staniland
Department of Chemistry
University of Sheffield
Brook Hill, Sheffield S3 7HF, UK

cancer research has rapidly expanded in the past 10 years and is now paving the way for various clinical trials.[2] However, the majority of these therapeutics rely on direct access to tumor site(s) for intratumoral administration. Although this can control the precise concentration of virus at the tumor site and thereby reduce side effects, the risks associated with complex procedures for intratumoral delivery make repeat dosing difficult[3] and renders this approach to be more suited to superficial tumors, such as melanoma. Equally, the variability in response following systemic administration of OVs[4] represents an unmet clinical need for patients with metastatic and inaccessible (e.g., brain, pancreatic) neoplasms.

Therefore, the delivery of efficacious concentrations of OVs into the tumor target following systemic delivery not only requires a navigation system over and above their endogenous tropism,[5] but also an immunosurveillance avoidance system to limit early clearance via the innate host antiviral immune system.[6] Neutralization and clearance of viruses from the bloodstream involves specific binding of antibodies or serum proteins, destruction via complement and immune cells and sequestration in organs such as the liver, spleen, and lungs.[7] Delivery of OVs to the tumor bed can also be affected by physical barriers such as the tumor extracellular matrix and high interstitial pressure which restricts extravasation.[8] Despite these obstacles, previous clinical trials have suggested that intravenous OVs can target tumors by using high doses of virus which saturate these neutralizing mechanisms.[9] The potentially devastating side effects of this saturation strategy can be mitigated against by disguising the OVs from the immune system, such as the use of whole cell Trojan horses.[10] However, again the reliance on passive tropism of cells results in a lack of specificity, presents challenges with respect to the delivery of the concentrations required to elicit significant efficacious responses and therefore risks abscopal toxicity. Equally, although liposomes,[11] dendrimers,[12] and polymeric nanoparticles[13] have demonstrated shielding and cell binding advantages,[14] the ultimate carrier must simultaneously provide active guidance.[6]

In this study, we combine the therapeutic activity of the OV (HSV1716) with nanomagnets (magnetosomes, MAG) isolated from specialized magnetotactic bacteria. This provides navigational properties for the magnetized HSV1716 complexes in the presence of a magnetic field. MAG also act as a coat of armor, shielding the OVs from neutralizing antibodies and thereby enabling higher concentrations to be delivered to the tumor target. Herein, we show that this approach reduces the in vivo growth of primary breast cancer and the development of metastasis in a pre-clinical murine model by replicating within and reprograming the tumor microenvironment (TME).

2. Results and Discussion

2.1. Magnetosomes Possess Unique Properties Ideal for Nanocarriers

Biologically derived magnetic nanoparticles called MAG were extracted from a well-characterized magnetotactic bacterial strain, *Magnetospirillum magneticum* AMB-1 (**Figure 1**a), following established protocols for their growth and maintenance.[15] These bacteria produce chains of cubooctohedral-shaped MAG (Figure 1b) with a mean diameter of 56.8 ± 0.4 nm (Figure 1c) and electrical surface charge of −34.54 ± 0.9 mv. Magnetic properties of MAG typically showed a coercivity of 1.9 kA m^{-1}, saturation magnetization of 220 kA m^{-1} and remanence of 63 kA m^{-1} (Figure 1d). Although magnetic susceptibility, χ, reduced with increased frequency (Figure 1e), as is commonly observed,[16] the decrease was more pronounced as MAG concentration increased and may indicate an increased level of agglomeration at higher concentrations.

Agglomeration of MAG at lower concentrations is mitigated against by the presence of a unique magnetosomal phospholipid membrane, as seen in Figure 1b. X-ray photoelectron spectroscopy (XPS) was used for the first time to characterize the magnetosomal membrane (Figure 1f). The elemental atomic % estimates from peaks in XPS wide scans of MAG detected phosphorous attributed to the phospholipids. The small iron signal suggests that general coverage of the magnetite core is good and tiny quantities near the surface of the MAG are more likely a gap in the phospholipid layer, rather than a very thin phospholipid layer. Additionally, the presence of endotoxins (22 endotoxin units μg^{-1} of MAG detected by LAL chromogenic ELISA) associated with the phospholipid layers of gram negative bacteria acted as a surrogate marker for the magnetosomal membrane. However, these toxins pose a potential clinical safety risk.[17] Rather than strip the magnetosomal membrane from the magnetite core and replace with polymers (e.g., PLL[18] and polyethyleneimine (PEI)[19]), as has been attempted by other investigators, we have been able to decrease endotoxin concentration using numerous removal techniques (Figure S1, Supporting Information). To maintain magnetosomal membrane patency 70% v/v ETOH was selected as the optimum sterilization technique, as this reduced endotoxin concentration by 69%, although endotoxins were not removed completely. NanoString amplification-free gene expression profiling of tumors from mice receiving either MAG or PBS (Figure S2, Supporting Information) further supports the presence of endotoxin and thus maintenance of the magnetosomal membrane, whereby the biological function of differentially expressed genes <0.05 were seen to be involved in the response to lipopolysaccharide (LPS). Mice tolerated treatment with MAG alone without any observable side effects suggesting that the amount of LPS present was below the threshold for toxicity. Interestingly, other studies have utilized the immunostimulatory effects of bacterial components that our NanoString data eludes to induce antitumor immunity in glioblastoma[20] and pancreatic carcinoma.[21] Conversely, LPS has also been implicated in enhancing prostate[22] and breast cancer[23] metastasis, clearly demonstrating the need to balance the inflammatory role of LPS for any future translation.

Maintenance of the magnetosomal membrane conferred other advantages including prevention of aggregation of magnetosomal suspensions as demonstrated by zetaview but it also facilitated evaluation of the tracking and magnetic capture capabilities of MAG both in vitro and in vivo by incorporation of the lipophilic dye DiD (1,1″-Dioctadecyl-3,3,3″,3′-Tetramethylindodicarbocyanine). Pharmacokinetics of intravenously delivered MAG was evaluated in blood samples

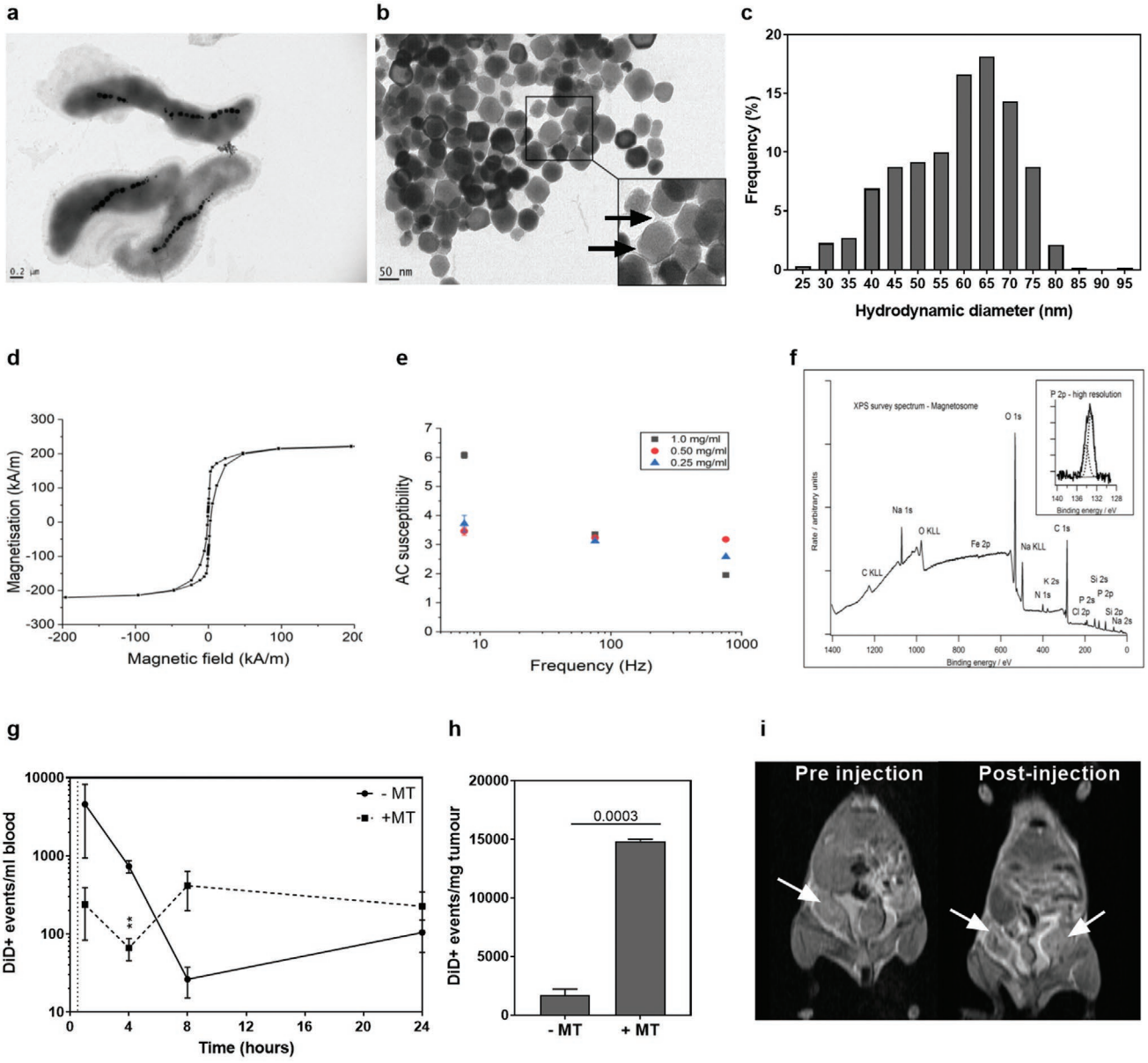

Figure 1. Characterization of AMB-1 MAG. Representative transmission electron microscope image of AMB-1 magnetotactic bacteria (a), purified AMB-1 MAG with magnetosomal membrane (inset, arrowheads) (b) and MAG size distribution histogram (c). Representative profiles of hysteresis loops (d) and magnetic (AC) susceptibility (e) of dried MAG. Representative XPS wide scan/survey spectrum of MAG with P 2p high resolution inset (f). Flow cytometric analysis of MAG concentration in the blood (g) and tumor (h) of mice following intravenous injection in the presence (■) and absence (●) of local magnetic targeting (MT) (g). Representative T2* weighted magnetic resonance images of tumor bearing mice (i) before (-MAG) and (ii) after intravenous administration of MAG. The paramagnetic properties of MAG cause a decrease in T2* relaxation time and therefore signal decreases where pooling occurs. We observed dark spots (arrowheads)within target tumors after administration (+MAG). In (c), size distribution was quantified from 5 independent TEM images at x17500 magnification. In (g,h) data are shown as mean ± SD ($n = 3$) per timepoint. Statistical significance was determined by *t*-Test.

collected from tumor-bearing mice 1, 4, 8, and 24 h postinjection. The concentration of MAG in the blood of control mice (-MT, magnetic targeting) reached a Cmax of 4581 ± 3645 DiD positive events 1 h postinjection and followed a typical IV bolus trajectory by decreasing rapidly over the subsequent timepoints (Figure 1g). Interestingly, in mice that were subjected to 30 min of magnetic targeting (+MT) within the tumor area, the curve demonstrated a statistically significant decrease in the number of DiD positive events in the blood ($p < 0.01$) 4 h postinjection, reaching a Cmax of 415 ± 215 DiD positive events at 8 h postinjection in comparison to control mice not exposed to magnetic trapping (-MT) (Figure 1g). Concomitantly, a statistically significant increase in the concentration of MAG in tumors 1 h postinjection was detected in mice that were subjected to magnetic trapping (1677 ± 532 vs 14 837 ± 152 DiD positive events mg^{-1} tumor, $p = 0.0003$) (Figure 1h), suggesting that magnetic

targeting facilitates MAG accumulation in breast tumors. A concomitant increase in DiD positive events/mg liver compared to blood suggests this is a major route for clearance of the MAG (Figure S3, Supporting Information). Additionally, events measured in the liver of mice subjected to magnetic trapping was reduced at the earlier timepoints (1 and 4 h) compared to those without, returning to normal levels by 8 h. This indicates the temporary sequestration of MAG by the tumor, although this is not significant.

Due to their enhanced relaxivity,[24] the biodistribution of MAGs can be tracked by spin-echo based magnetic resonance imaging (MRI) pre- and postintravenous injection (Figure 1i). Alongside increased detection in tumor tissue, MAG uptake was found in major excretory organs such as the kidneys (Figure S4, Supporting Information). Alongside use as contrast agents for potential diagnosis, MAG have proven invaluable in stem cell[25] and magnetic fluid therapy for the destruction of tumors and so can be considered as "theranostics".[26] Indeed, we have demonstrated, using in vitro vascular models, that our MAG can be "steered" in a particular direction with MR targeting (Figure S5, Supporting Information) therefore acting as a potential route to further increase therapeutic efficacy, in line with our previous work.[27,28]

The in vitro properties of the MAG demonstrated that despite incomplete removal of endotoxins, no cytotoxicity against a panel of human and mouse derived breast cancer cell lines when incubated with 0.5 mg mL^{-1} for 5 days was observe d (Figure S6, Supporting Information).

Cellular uptake of 0.1 mg mL^{-1} DiD-labeled MAG was cell line-specific, with murine E0771 cells demonstrating a sixfold increase compared to 4T1 (Figure S7a, Supporting Information), whereas MAG uptake by human MDA-MB-231 cells was twofold greater than that by human SKBR3 cells. The differences in cell specific uptake of MAG displayed are not statistically significant but potentially demonstrate inherent tissue tropism. Iron oxide nanoparticle uptake has been demonstrated to be more pronounced in cancer cells over healthy cells[29] with different uptake velocities and behaviors exhibited by different cancer cell lines.[30] Higher uptake of iron oxide nanoparticles by MDA-MB-231 compared to MCF7 cells is evidenced[30,31] and is thought to be associated with the invasiveness of cancer cells. The invasive potential of MDA-MB-231 cells rank higher than SKBR3 cells, measured by both the Boyden chamber method[32] and more recently the mitochondrial redox ratio,[33] correlating with this study's findings that more invasive MDA-MB-231 cells more readily internalize MAG in comparison to less invasive SKBR3 cells. The same cannot be said for murine cells lines used in this study as both represent invasive phenotypes. We therefore sought to investigate whether the tropism was associated with LPS interactions with cancer cell membrane components, possibly via the LPS-CD14-TLR4 endocytosis pathway (Figure S7b, Supporting Information) resulting in activation of innate immune cells as part of host-pathogen interactions. We evaluated expression of CD14 and TLR4 by flow cytometry (Figure S7b–d, Supporting Information). A pattern of expression per species was noted with human cells displaying CD14-/TLR4+ expression while mouse cells were predominantly CD14+/TLR4-. There was no difference in TLR4 expression between human cell lines but 4T1 cells demonstrated a statistically significant increase in CD14 expression compared to E0771 cells ($p = 0.0008$). CD14 has a protective role and is required for host defence in models of gram-negative respiratory infections which could explain the decrease in magnetosomal uptake by 4T1 cells. Additionally, the fate of nanoparticles can be driven by a number of factors that relate to the mechanism of internalization with endocytic pathways including macropinocytosis, clathrin, and caveolin dependent and actin-independent known to be modified in cancer.[34] Crucially, regardless of their intrinsic capabilities, MAG internalization by all cell lines was increased by incubating for 1 h in the presence of a plate magnet ($p < 0.05$) (Figure S6a, Supporting Information) and was further influenced by MAG concentration and incubation time (Figure S8, Supporting Information).

These results indicate that MAG confer many desirable properties as potential nanocarriers including a uniform nanoparticle distribution, low toxicity, a stable magnetic moment as well as ferromagnetic behavior allowing MR imaging and magnetic targeting. Additionally, a biologically compatible membrane prevents aggregation and confers natural binding properties for therapeutic attachment and fluorescent labeling.

2.2. Characterization of MAG-OV Demonstrates Oncolytic and Shielding Properties

Complex formation between HSV1716-GFP with the biologically inert, but magnetically susceptible AMB-1 MAG was generated by exploiting the electrostatic differences between the two components (Table S1, Supporting Information) to create a magnetized virus (MAG-OV) (**Figure 2**a). MAG-OV demonstrated a hydrodynamic diameter of 160 ± 20 nm comprising a central virus particle surrounded by smaller MAG, forming clusters of complexes (Figure 2b). Within MDA-MB-231 cells, DiD-labelled MAG, and GFP-expressing OV of MAG-OV complexes demonstrated co-localization (Figure 2c) and high-powered transmission electron microscopy (TEM) imaging indicated MAG-OV localized in the cytoplasm or in the endosomes of the cells (Figure 2d). Free virus particles were seen throughout the cytoplasm, whereas MAG alone located in the endosomes, suggesting that once inside the cell the virus is able to free itself from the complexes. To further confirm the interactions between the virus and MAG, the detected elemental atomic% (Figure 2e) were estimated from the peaks in XPS wide scans (Figure 2f). Using the XP spectra from the virus and MAG as references, the MAG-OV spectra were modelled (Figure 2g–i) for nitrogen (N 1s). The peak fit to the virus spectral envelopes (Figure 2g) and the peak fit to the outer layer of the phospholipid membrane on the MAG (Figure 2h) were combined in the MAG-OV spectrum (Figure 2i) indicating the presence of both virus and MAG, amounting to ≈29% virus signal versus 71% MAG surface signal.

The effective oncolytic activity of MAG-OV complexes was comparable to OV alone (multiplicity of infection, MOI 10) in both monolayer (**Figure 3**a) and tumor spheroid cultures (Figure 3b,c). However, magnetic targeting of MAG-OV at a much lower MOI (0.01) induced a twofold decrease in cell viability of MDA-MB-231 cells (Figure 3d) demonstrating potential for lower, safer, viral concentrations without compromising

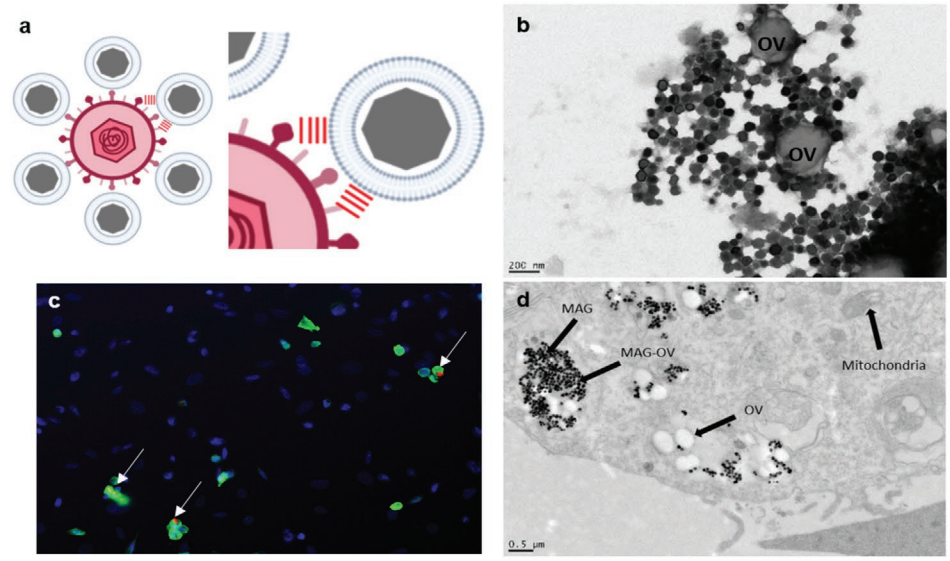

e

Peak/Sample (%)	OV	MAG	MAG-OV
C 1s	44.8	51.4	51.7
O 1s	23.0	29.1	29.3
N 1s	4.7	1.8	3.0
Na (KLL)	13.6	6.1	1.0
P 2p	2.6	2.9	0.8
Fe 2p	0.0	0.1	0.2
Cl 2p	8.8	0.7	0.6

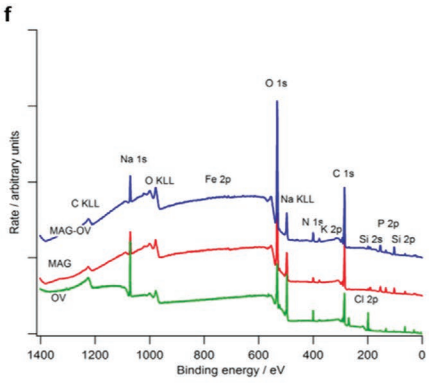

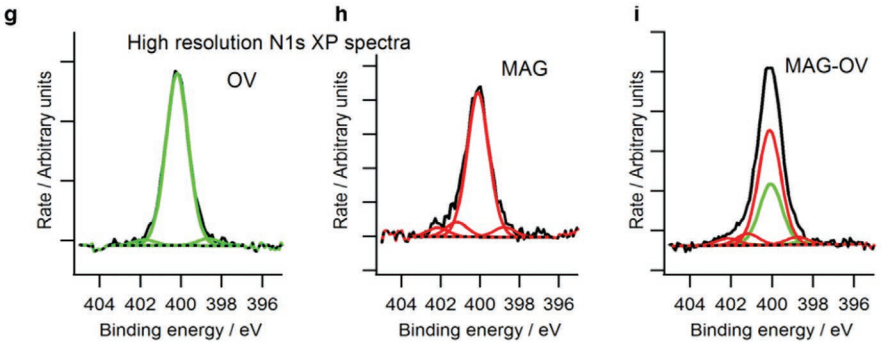

Figure 2. Characterization of MAG-OV complexes. Schematic proposing MAG-OV complexation of oncolytic virus (HSV1716) with a protective layer of MAG via electrostatic interactions (red lines) (a). Representative transmission electron microscope images of MAG-OV complexes in PBS suspension (b). Representative fluorescent image of DiD labeled MAG (red) colocalized with GFP-expressing HSV1716 (green) in infected MDA-MB-231 monolayers (c). Representative transmission electron microscope images of MAG-OV complexes within MDA-MB-231 tumor cells (d). Estimated atomic % of detected surface elements (e) from XPS survey spectrum (f) for each treatment. Representative N 1s high resolution XP spectra from OV (g), MAG (h), and MAG-OV (i) treatments. Peak fits for the magnetosomal membrane (red) and virus (green). All spectra charge corrected to aliphatic carbon, C 1s at 285 eV. In (e) data are shown as the mean of wide scans on three areas of each sample. SD are < ± 2 at% for abundant elements, ≈± 0.1 at% for less abundant ones.

efficacy. Susceptibility to viral infection is cell line-dependent (Figure S9, Supporting Information), yet magnet induced uptake of MAG was significantly enhanced even in the most resistant cancer cells (4T1, Figures S7 and S8, Supporting Information), suggesting that combining MAG-OV with magnetic targeting may overcome poor viral cell entry into these cells. As well as

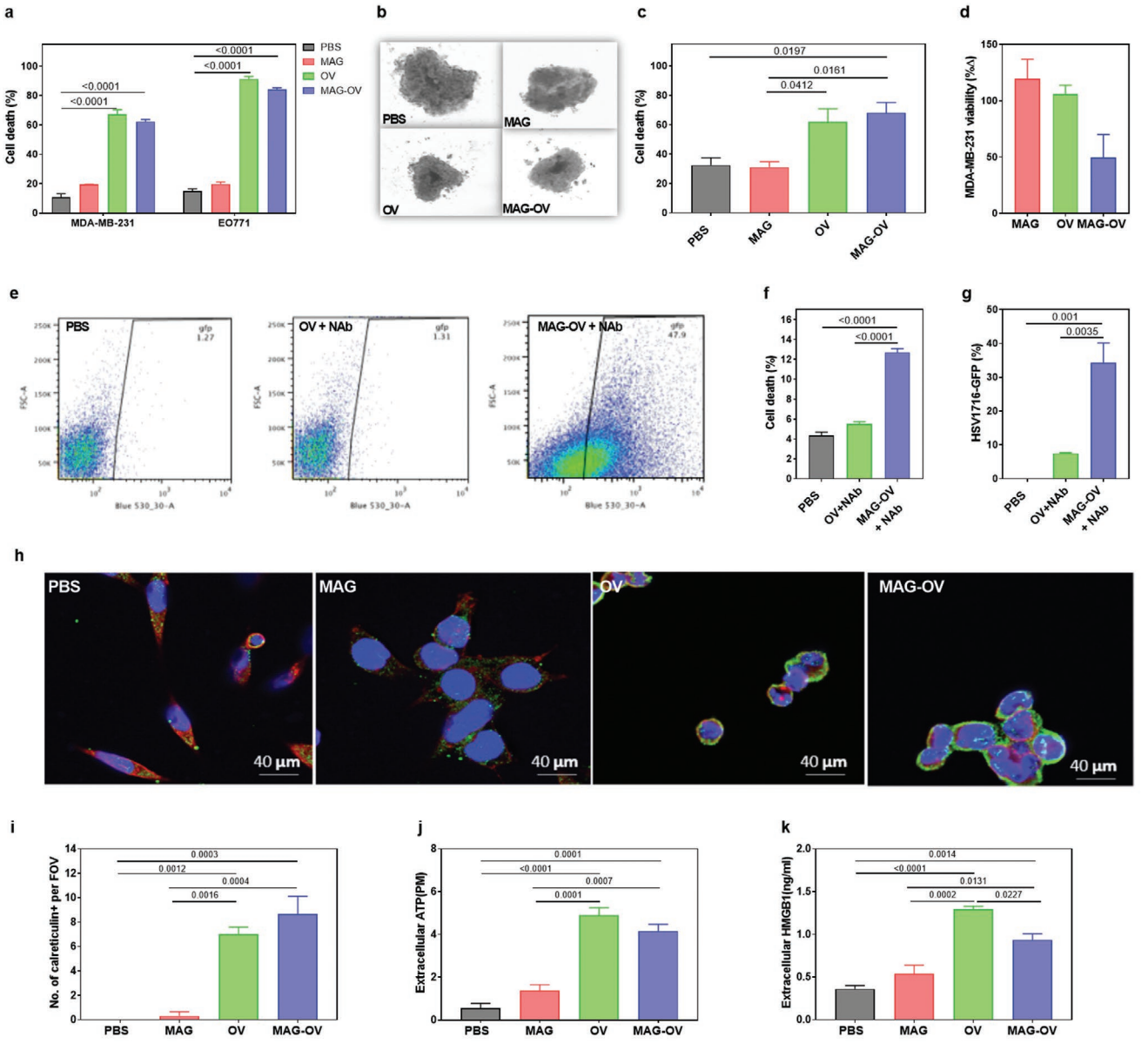

Figure 3. MAG-OV are protected from neutralizing antibodies and are more cytotoxic than virus alone in vitro. Relative percentage cell death of MDA-MB-231 and E0771 cells after different treatment for 120 h (MOI 10) (a). Relative percentage cell death of MDA-MB-231 spheroids after different treatment for 72 h (MOI 10) (b,c). Relative cell viability of MDA-MB-231 cells after different treatment + magnetic targeting (MOI 0.01) (d). Total percentage cell death (e,f) and total HSV1716-GFP expression (e,g) of MDA-MB-231 cells after 24 h different treatment co-incubated with neutralizing antibodies. Total number of CRT positive MDA-MB-231 cells (red) per field of view (FOV) after different treatment for 24 h (HSV1716, MOI 10, green) (h,i). Extracellular concentration of ATP (j) and HMGB1 (k) from culture media 24 h after different treatment (MOI 10). Data are shown as mean ± SD with experiments independently repeated three times. Statistical significance was determined by one-way ANOVA with a Tukey post hoc test.

enhancing cell uptake, the MAG shell also prevented neutralization of the virus in the presence pre-existing immunity, resulting in a significant increase in MDA-MB-231 infection and cell death in the MAG-OV group compared to OV alone ($p < 0.0001$) (Figure 3e–g). Mechanisms for the enhanced oncolytic activity of MAG-OV are attributed to direct cell lysis, as evidenced by a significant increase in genes upregulated during viral replication (gB, ICP0 &ICP8) (Table S2, Supporting Information), and the induction of immune cell death characterized by the secretion of ATP andHMGB1 and expression of calreticulin (CRT).[35]

CRT located in the cytoplasm translocates and co-localizes with HSV1716 at the nucleus 24 h after infection with both OV and MAG-OV (Figure 3h). As well as a change in distribution, CRT expression was induced sevenfold (<0.001) and ninefold (<0.0001) by OV and MAG-OV respectively compared to PBS controls (Figure 3i). OV and MAG-OV treatment also increased concentrations of secreted (extracellular) ATP (Figure 3j) and HMBG1 (Figure 3k). Additionally, the profile of pro- and anti-inflammatory gene expression was similar in both OV and MAG-OV treated cells, in which genes involved in ICD (IFN-ϒ,

HSPA1A, NF-$\kappa\beta$, and TNF-α), nonICD (LC3B) and apoptosis (CASP3 and CASP8) were significantly upregulated, whereas the expression of genes normally associated with tumorigenesis (HSP90AA1 and VEGF) were significantly downregulated (Table S2, Supporting Information). Interestingly, there was a statistically significant difference in CASP3, LC3B, and TGF-β gene expression in OV and MAG-OV treated cells which might represent enhanced cell death mechanisms due to increased viral replication. Equally, cytokine bead arrays corroborated the antitumor properties of OV and MAG-OV, in that the secretion of CXCL10 (a chemoattractant for inflammation and marker for poor prognosis), IL-6 (promotes tumor growth), IL-8 (involved in cancer related inflammation), and VEGF (responsible for neovascularization of tumors) was significantly downregulated in these treatment groups (Figure S10, Supporting Information).

2.3. MAG-OV Enhances Survival by Stimulating ICD in Primary Mammary Cancer

The in vivo antitumor efficacy of MAG-OV after 30 min of magnetic targeting (MAG-OV+MT) was investigated in an orthotopic breast tumor mouse model implanted with E0771 cells (**Figure 4**a). Treatments had no observable adverse effects (Figure S11, Supporting Information). MAG-OV+MT exhibited a greater capacity to inhibit tumor growth than the other treatment groups and thereby enhanced survival (Figure 4b). Whereas a median survival of 12 days was observed for PBS, MAG, and MAG-OV treated mice and 15 days for OV treated mice, this was 21 days for MAG-OV+MT treated mice ($p < 0.0001$ vs PBS and $p = 0.0002$ vs OV, Log-rank test). MAG-OV+MT not only decreased primary tumor volume (Figure 4c; and Figure S11b,c, Supporting Information), but also enhanced protection from the development of lung metastases (Figure 4d) and hence overall tumor burden. Further tissue analyses were performed without MAG-OV group as this showed no difference to OV alone (Figure 4b,c).

A 4.6-fold increase in OV expression correlated with a decreased CD31 expression and increased cell death, as measured by increased expression of CRT protein and necrosis, was observed in the tumors after MAG-OV+MT treatment (Figure 4e–i). CRT is a multicompartmental protein that regulates a wide array of cellular responses important in physiological and pathological processes[36] including ICD. High levels and subcellular localization of CRT as we have seen in Figures 3h and 4e could be a result of hypoxic conditions which induces CRT overexpression; oxidative damage or posttranslational modifications; lower calcium levels in the ER resulting in CRT translocation as well as its release from cells by necrosis. Additionally, when combined with evidence of upregulation of heat shock proteins (Table S2, Supporting Information) suggests evidence of a stress response that warrants further investigation.

In a separate study, direct tumor cell lysis by OV in tumor bearing C57BL/6 mice was evidenced by the release of intracellular fluid rich in phosphate and uric acid due to the rapid release and metabolism of intracellular nucleic acids, as well as biochemical evidence of rapid tumor lysis by measurement of AP, ALT, and AST[37] (Figure S12, Supporting Information).

These findings suggest that magnetic targeting combined with OV can enhance efficacy by disrupting tumor vascularity as well as inducing direct and indirect cytotoxic effects. Most promisingly, we showed that MAG may help to overcome the issues surrounding nonspecific biodistribution of OVs by utilizing their magnetic properties for magnetic targeting under the use of an external magnetic field. Functionalizing nanoparticles represents a "targeted" approach for enhanced tumor recognition and cell entry yet crucially they all rely on passive transport for systemic delivery. Although the enhanced permeability and retention (EPR) effect is widely held to increase nanotherapeutic delivery to tumors over normal organs owing to their defective tumor vasculature, the heterogeneity of the EPR effect in cancer[38] often offers less than a twofold increase in nanodrug delivery compared with critical normal organs, resulting in drug concentrations that are not sufficient for curing most cancers.[39] We demonstrated enhanced viral infection of tumor cells in both monolayers and spheroid cultures in the presence of a magnetic field as seen previously where this technique has potentiated the efficacy of gene delivery vectors up to several hundred-fold.[40] Importantly, cell uptake was enhanced in breast cancer cell types that demonstrated poor passive uptake (4T1). Few studies have translated these results in vivo and whilst Tresilwised et al. did show a 10-fold increase in viral uptake in multidrug resistant and CAR-deficient tumor cells compared to nonmagnetic oncolytic Ad in the presence of a magnetic field,[41] the therapy was directly delivered intratumorally. We present one of the first studies to deliver a magnetic virus systemically, providing circulatory protection from immunosurveillance and active magnetic targeting at the tumor site for enhanced viral infection.

2.4. Induction of Immunomodulatory Effects

The NanoString nCounter PanCancer Pathways Panel was used to compare the cellular immune mechanisms employed by E0771 tumor cells following virotherapy (Figure 4a). A total of 252 genes were found to be differentially expressed in the MAG-OV+MT treated tumors to a p-value of <0.05 when compared with PBS-treated tumors (**Figure 5**a). Of these, the expression of 207 genes were increased and that of 46 genes decreased. The 20 genes found to exhibit the greatest change in expression were associated with the innate and adaptive immune responses, adhesion, T cell function, apoptosis, and inflammation (Table S3, Supporting Information). As individual genes can be involved in multiple pathways, the overall effect of these genes was investigated using the Database for Annotation, Visualization and Integrated Discovery (DAVID) which categorizes genes into groups depending on their biological function (Figure 5b).[42] The inflammatory response was the function with the highest gene count (73), followed by the immune system (68 genes), and apoptosis (61 genes). It was interesting to note that of the top 20 differentially expressed genes for each treatment group, GlyCAM-1, CD19, and Pax-5 were significantly upregulated in OV (Table S4, Supporting Information) treated animals, yet significantly downregulated in MAG-OV+MT when compared to PBS controls. These genes all have roles in B cell lymphocyte recruitment and development. In addition,

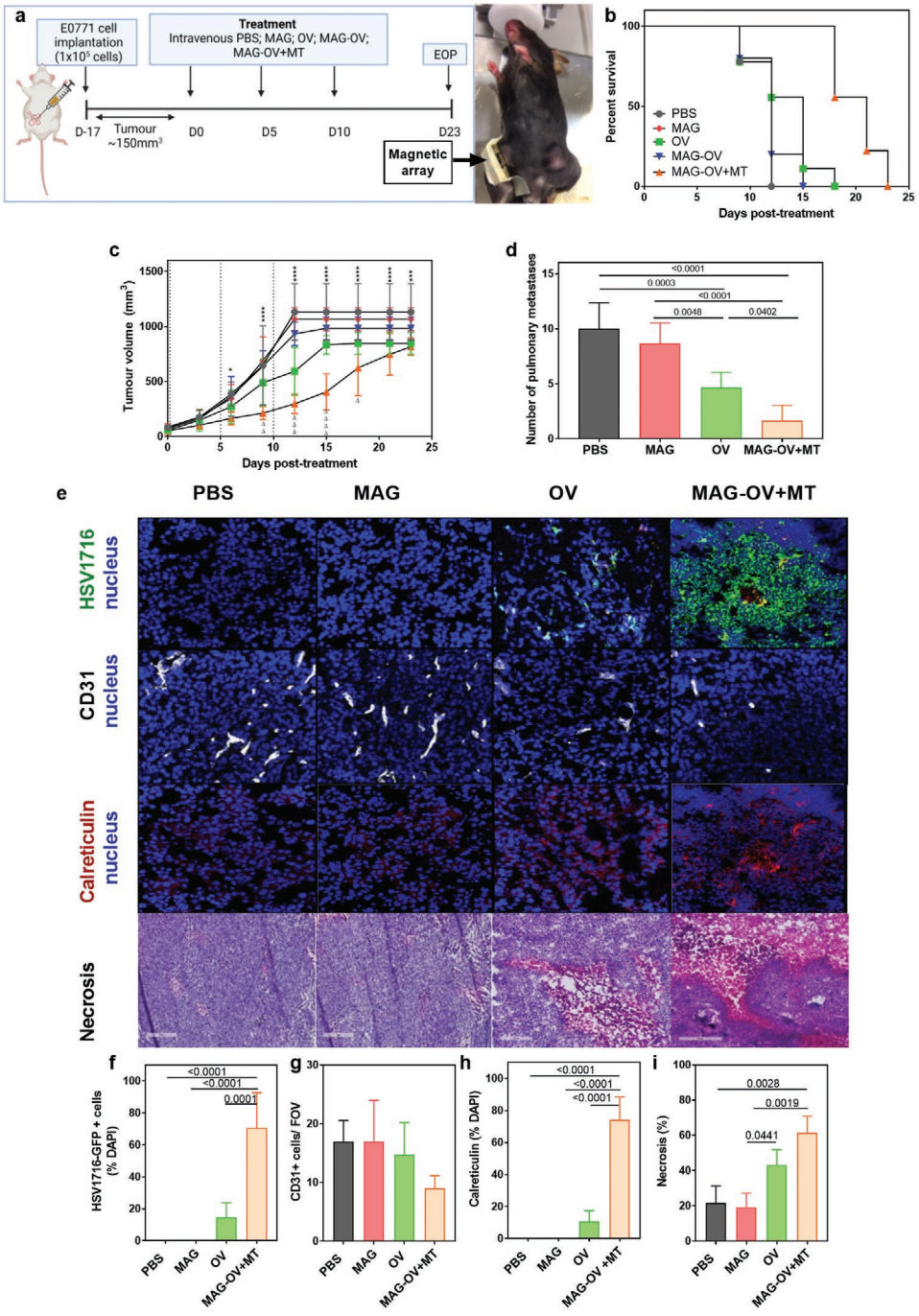

Figure 4. Magnetic targeting of MAG-OV reduces overall tumor burden in vivo. C57/Bl6 mice received different treatments on days 0, 5 and 10, once average tumor size had reached 100 mm^3 (a, created using BioRender) (EOP = End of Procedure.). Magnetic targeting was achieved using a 0.7T magnetic array attached to the tumor for 30 min. Percentage survival (b), tumor volume (c), and number of pulmonary metastases (d) after different treatments. HSV1716-GFP (e,f), CD31 (e,g), and CRT (e,h) expression by tumor cells following different treatment was observed using immunofluorescent labeling and necrosis was observed by H&E staining (e,i). In (c,d), (f–i), data are shown as mean ± SD. ($n = 9$ in b–d); $n = 3$ in f–i). In (c), statistical significance was determined by Two-way ANOVA with repeated measures following Last Observation Carried Forward where * = PBS versus MAG-OV +MT and Δ = OV versus MAG-OV +MT. In (g–i) statistical significance was determined by one-way ANOVA with a Tukey post hoc test.

we identified gene expression for relative (Figure 5c) and raw abundance (Figure 5d) of tumor infiltrating immune cells. The Nanostring data demonstrate significant increases in NK cells ($p < 0.001$) including $CD56^{dim}$ NK cells ($p < 0.01$), T cells ($p < 0.05$) including cytotoxic T cells ($p < 0.01$), and $CD8^+$ T cells ($p < 0.01$), macrophages ($p < 0.05$), and neutrophils ($p < 0.05$), with a concomitant decrease of B cells in tumors treated with MAG-OV+MT compared to OV. The genes of interest identified

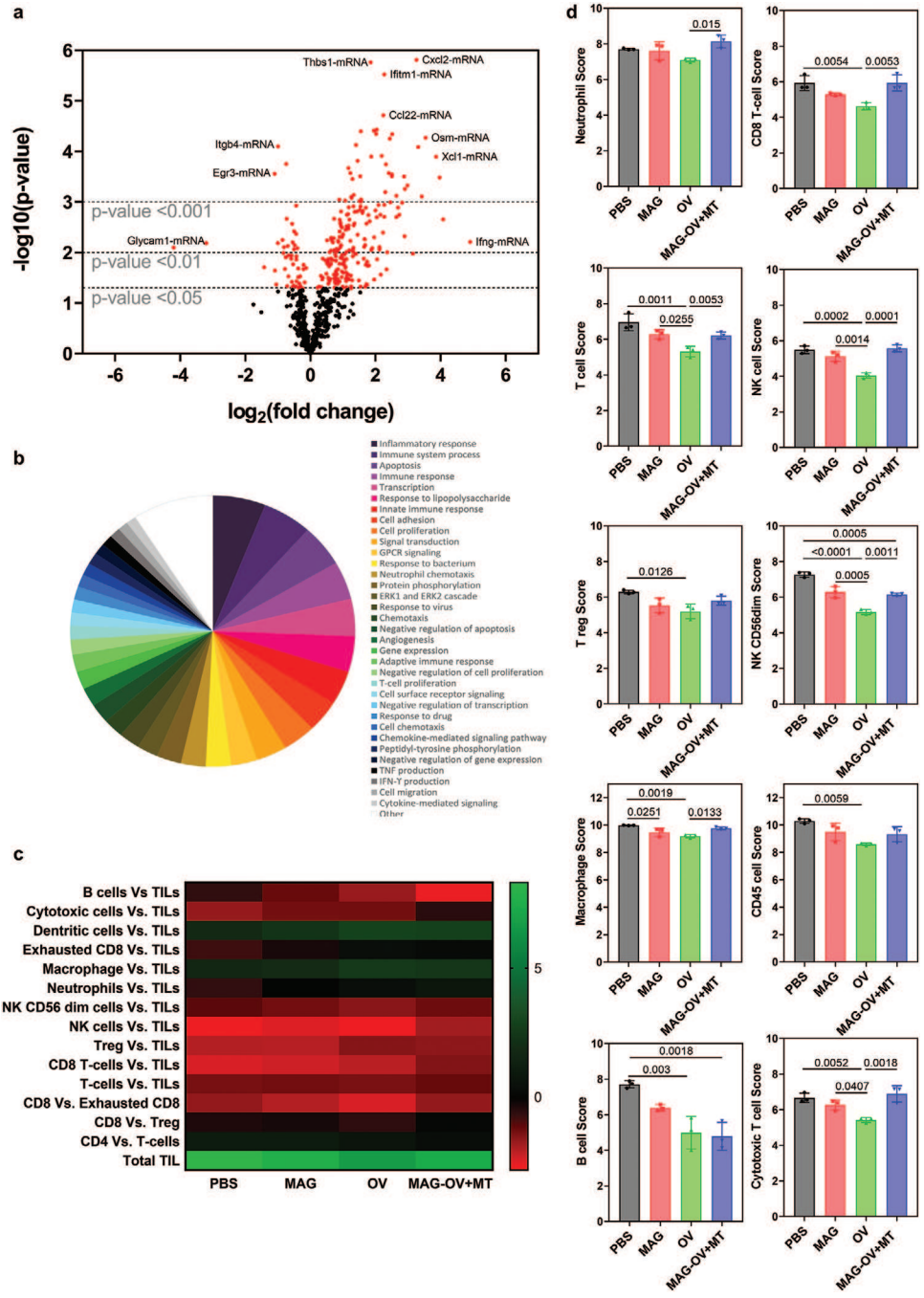

Figure 5. MAG-OV+MT upregulates expression of immune related genes. Differential expression of immune related genes (a). Data expressed as log2 fold change in the gene expression of MAG-OV+MT versus PBS control groups, where each data point represents one gene. Change in gene expression $p < 0.05$ represented by red datapoints ($n = 3$). DAVID analysis describing the biological functions of differentially expressed genes $p < 0.05$ (b). The relative abundance of each immune cell type after different treatment (c) was calculated by subtracting the total tumor infiltrating lymphocyte (TIL) score (an average of the B cell, T cell, CD45, macrophage and cytotoxic cell scores) from each single cell type score. Raw abundance of TILs after different treatment d). In (d), data are shown as mean ± SD ($n = 3$). Statistical significance was determined by one-way ANOVA with a Tukey post hoc test.

in Figure 5 were examined by immunofluorescence and flow cytometry whereby an increase in the number of NK cells and $CD8^+$ T cells within MAG-OV+MT treated tumors (**Figure 6**; and Figure S13, Supporting Information) and their increased presence alongside activation markers IFN-γ and PD-1 (Figure 6) suggests a T cell-mediated antitumor response which enhances the survival of mice bearing EO771 cell line-derived tumors. Of note, by flow cytometry CD8 T cell population demonstrated significant increase over PBS but not OV alone where there was trend.

This combination of enhanced active viral replication within the tumor and stimulation of an antitumor immune response

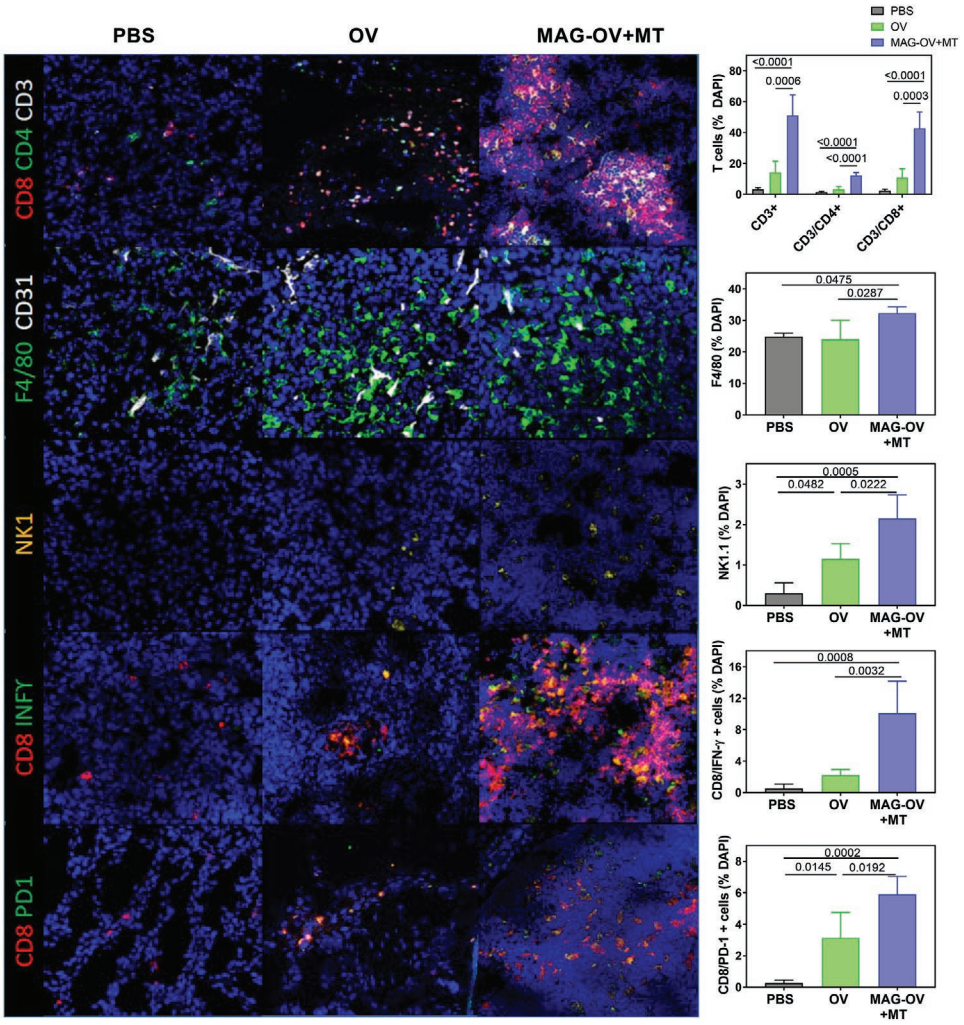

Figure 6. MAG-OV+MT stimulates a T lymphocyte-mediated antitumor response. Representative images of EO771 tumor sections examined by terminal immunofluorescent staining and their quantification of signals for T cells (CD8/CD3/CD4 ratios), natural killer T cells (NK) and macrophages (F4/80) as well as the co-localization of cytotoxic T cells with interferon (CD8/INFɣ) and programmed cell death protein 1 (CD8/PD1). Data are shown as mean ± SD ($n = 4$). Statistical significance was determined by one-way ANOVA with a Tukey post hoc test.

has been described in clinical trials using T-Vec as a monotherapy for melanoma.[43] Whilst this study resulted in a 50% increase in survival, we were unable to completely eradicate the tumor and following cessation of treatment, tumor growth resumed. A similar pattern was seen following intratumoral injection of poliovirus in a melanoma model[44] and feeds into the argument that "repeat dosing is essential for the success of oncolytic virotherapy."[45] Subsequently, the clinical landscape is predominantly focused on combinatory treatments with OVs including a recent treatment for nonmetastatic triple negative breast cancer (TNBC) whereby intratumoral T-Vec enhanced patient response to neoadjuvant chemotherapy via stimulation of TILs.[46] Alternatively, sustaining the anti-tumor response may also rely on improvements in the formulation and hence stability of MAG-OV complexes. We have demonstrated that storage for 3 days at 4 °C (Figure S14a, Supporting Information) revealed no impact on virus viability as determined by plaque assay (ns, paired T-test). Overall the data presented suggest that the electrostatic interactions of the complexes are surprisingly stable, however their chemical stabilization using cross-linkers represents an opportunity for further optimization and potential to increase the efficacy and duration of response seen in this study.

3. Conclusions

Most clinical subtypes of breast cancer are considered to be immunologically "cold" (less likely to engage the immune system) making them unresponsive to immunotherapies.[47] OVs represent a new immunotherapy with the potential to stimulate the immune system and elicit cell-mediated antitumor immunity by reprogramming tumors to become "hot" (readily engage the immune system). However, improving the efficacy of OVs requires formulations that have a safe carrier, an active targeting component and an improved exposure profile. We have developed a nanotherapeutic strategy harnessing the power of "bugs as drugs," whereby magnetic targeting of

bacterially derived MAG promote the delivery of OVs by overcoming the challenges associated with systemic access to advanced, disseminated tumors. This novel biotechnological approach clearly demonstrates that our MAG-OV complex allows multiple levels of specific tumor targeting by reducing systemic exposure and increasing accumulation in solid tumors via evasion of immunosurveillance and magnetic targeting. Moreover, MAG-OV elicits on-target, off-tumor T cell-mediated eradication of primary tumors and metastatic lesions. These findings advocate for the combination of bacterial and viral components in the creation of "bugs as drugs," to increase the therapeutic index of systemically delivered OV, thereby supporting its future use for treating a wide range of inaccessible malignancies.

4. Experimental Section

Animals: Experiments were carried out in 6–8 week old female C57BL/6 or FVB mice (Charles River, UK) maintained on a 12:12 h light/dark cycle with free access to food and water. Experiments were carried out in accordance with local guidelines and with UK Home Office approval under project licenses 70/8670 at the University of Sheffield, UK.

Cell Lines: Human breast cancer MDA-MB-231 (European Collection of Authenticated Cell Cultures (ECACC), SKBR3 (American Type Culture Collection, *ATCC) and* mouse mammary cancer cells EO771 (obtained from Dr Jessalyin Ubellacker (Harvard University, USA), PyMT-TS1 (ATCC) and 4T1 (ATCC) were cultured in DMEM growth medium supplemented with 10% v/v fetal bovine serum (FBS, Gibco, Invitrogen, Paisley, UK), in a humidified incubator under 5% v/v CO_2. E0771 and PyMT-TS1 cells were stably transfected to express luciferase cultured in DMEM + 10% FCS (Gibco, Invitrogen, Paisley, UK). The identities of all cell lines were regularly confirmed using microsatellite analysis and were tested to be mycoplasma free.

Viruses: HSV1716 and GFP expressing HSV1716 were obtained from Virtuu Biologics Ltd in stocks of 1×10^8 Particle Forming Units (pfu) in compound sodium lactate (Hartmann's solution) with 10% v/v glycerol. HSV1716 is derived from HSV strain 17+ with deletions of both copies of the RL1 gene encoding for the neurovirulence factor ICP34.5 (HSV1716). HSV1716-GFP has a green fluorescent protein (GFP) added to the RL1 gene locus and is driven by the phosphoglycerate kinase (PGK) promoter.[48] All vials were stored at −80 °C and freshly thawed on ice in 0.1 mL aliquots immediately before each experiment. All in vitro experiments were performed at an MOI of 10 unless otherwise stated.

Bacterial Culture and Magnetosome Preparation: *Magnetospirillum magneticum* AMB-1 (kindly provided by the Matsunaga group, Tokyo Institute of Agriculture and Technology) was cultivated microaerobically (1% v/v O_2, 99% v/v N_2, 30.1 °C) in loose-capped 1 liter bottles of culture medium. This medium contained (per liter of deionizer water) 1.36 g KH_2PO_4, 0.74 g L(+)-Tartaric acid, 0.1 g Na-acetate, 0.24 g $NaNO_3$, 0.74 g succinic acid, and 1 mg resazurin. The medium was autoclaved after adjustment of the pH to 6.75, after which autoclaved Na-thioglycolate (0.05 g), Wolfer's mineral solution (1.25 mL), Wolfer's vitamin solution (2.5 mL), and ferric-quinate (20×10^{-6} M) were added under sterile conditions. MAG were extracted from AMB-1 bacteria by cell lysis using microprobe tip sonication for 1 h and MAG were collected (magnetic separator rack; Invitrogen), washed [10×10^{-3} M Tris-HCl buffer (pH 7.4)] and stored in Dulbecco's phosphate buffered saline (DPBS) at an optical density (OD_{565}) of 1 .2 at 4 °C (equal to 1 mg mL^{-1}). Prior to use, MAG were sterilized in 70% v/v ethanol for 30 min in an ice-cold sonicating water bath, washed in DPBS and resuspended in sterile water. Fluorescently labeled DiD MAG were prepared by incubating 100 µg of MAG with 5 µL of Vybrant DiD cell labeling solution (Thermo Fisher) for 30 min at 37 °C, 100 rpm. MAG were washed 3 times with DPBS to remove excess dye and resuspended in sterile water.

Complex Preparation and Characterization: MAG-OV complexes were created utilizing electrostatic interactions between the two components as follows. Suspensions of sterilized MAG and HSV1716 were created in DPBS, incubated for 20 min at room temperature on a shaking platform (150 rpm) and used immediately for complex characterization (0.1 mg mL^{-1} MAG and 1×10^8 pfu mL^{-1} OV) or in vivo studies (0.2 mg mL^{-1} MAG and 1×10^8 pfu mL^{-1} OV).

For conventional transmission electron microscopy (TEM) analysis, either unstained samples or virus-containing samples stained with 1% v/v phosphotungstic acid were adsorbed on carbon-coated copper grids. TEM micrographs were acquired at a nominal magnification of x6500. For visualization of MAG-OV infected MDA-MB-231 (10^5) tumor cells, a 3% v/v glutaraldehyde in 0.1 M Sodium Cacodylate buffer, followed by a 2% v/v aqueous osmium tetraoxide fixation schedule was used. The cells were dehydrated in a series of aqueous ETOH solutions (v/v 75–100%), cleared in propylene oxide (PO), and infiltrated in a 50% mixture of PO/Araldite resin before a final infiltration with pure Araldite resin. Araldite resin blocks were cured at 60 °C for between 48 and 72 h before sectioning using a Leica UC6 ultramicrotome (Leica UK). Ultrathin sections (≈85 nm) were collected onto polymer-coated copper grids and stained using 3% v/v aqueous uranyl acetate and Reynold's lead citrate. MAG diameters were determined from TEM micrographs (n = 5) acquired at a nominal magnification of x18 500 and manually measured using Image J software. Samples from both techniques were examined using an FEI Tecnai T12 Spirit TEM (Thermo Fisher Scientific, UK) operated at 80 kV with an Orius 1000B digital camera and Digital Micrograph software (Gatan UK).

Zeta potential analysis of individual components (MAG and OV) and the MAG-OV complexes was performed in suspensions of ddH_2O at room temperature using a Particle Metrix ZetaView (Analytik, UK) with settings fixed to 2 (high) and frame rate 7.5. Three independent readings were performed per sample.

Magnetic measurements were performed on aqueous suspensions of MAG at concentrations of 0.25, 0.50, and 1.0 mg mL^{-1}. For this, 20 µL of a suspension was used to fill a polycarbonate capsule, which was then sealed to ensure no leakage prior to or during measurement. MAG-free water-filled capsules were also prepared to obtain background signals for subtraction from measurements of MAG samples. A Quantum Design MPMS3 superconducting quantum interference device—vibrating sample magnetometer (SQUID-VSM) was used to perform magnetic measurements with samples held at room temperature. Quasistatic (direct current "DC" mode) hysteresis loops were obtained with 10 s wait time per magnetic field value. Magnetic susceptibility was measured using the magnetometer's alternating current "AC" mode with an oscillating magnetic field of 40 A m^{-1} amplitude at frequencies of 7.57, 75.7, and 757 Hz, and zero DC field.

Characterization of the surface of complexes including elemental composition and bond kinetics were compared with each individual component using a Kratos LiPPS XPS instrument. Briefly, samples were mounted onto glass cover slips and allowed to air dry, after which they were mounted onto a standard Kratos sample bar using double sided tape and inserted into the instrument after prepumping down to a suitable vacuum in the airlock (the analysis chamber pressure was better than 5×10^{-9} mbar). Samples were analyzed using a Kratos AXIS ULTRA XPS instrument with a mono-chromated Al kα X-ray source (1486.6 eV) operated at 10 mA emission current and 12 kV anode potential (120 W). Spectra were acquired with the Kratos VISION II software. A neutralizer filament was used to prevent surface charging. Hybrid–slot mode was used measuring spectra from three separate areas per sample measuring ≈300 × 700 µm each. For each, a wide/survey spectrum at low resolution (binding energy range 1400 to −5 eV, with pass energy 80 or 160 eV, step 0.5 or 1 eV, sweep time 20 min) was used to estimate the total atomic% of the detected elements. High resolution spectra at pass energy 20 eV, steps of 0.1 eV, and sweep times of 10 min each were also acquired for photoelectron peaks from the detected elements, and these were used to model the chemical composition. The high resolution spectra were charge corrected to the C 1s peak (adventitious carbon or a known polymer $CH_{2\ or}$ CH_3 peak) set to 285 eV. Peak models were

created using a linear background and GL(30) component peak shapes unless otherwise stated. Casaxps (version 2.3.19 PR1.0 or later) software was used for quantification and spectral modeling.

MRI: Magnetic Resonance Imaging (in vivo) and targeting (in vitro) used a small bore 7 Tesla magnet (Bruker BioSpec Avance III 70/30, Bruker BioSpin, GmbH, Ettlingen, Germany) with preinstalled, actively shielded, 120 mm inner diameter, water cooled, gradient coil (Bruker BioSpin MRI GmbH B-GA12s. 660 mT m^{-1} maximum strength per axis with 4570 T m^{-1} s^{-1} slew rate). In vivo imaging employed a 1 H volume resonator (Bruker, 300 MHz, 1 kW max, outer diameter 118 mm per inner diameter 72 mm). The animal breathing rate was monitored using a pressure sensitive pad (SAII, USA—Model 1025L). Rectal temperature was measured using a thermocouple (SAII, USA—Model 1025L) and body temperature maintained using a heated water pump bed. Animals were anaesthetized with isoflurane (1.5% v/v in medical O_2, 2 L min^{-1}). Multiple gradient echo images were captured pre and post MAG i.v. injection.

In vitro magnetic resonance targeting experiments utilized a bifurcating vessel phantom. The phantom consisted of a bespoke in-house fabricated polydimethylsiloxane (PDMS) based microfluidic device.[49] In short, microchannels representing a simple bifurcating vessel system (<400 µm diameter) were milled in a block of acrylic. The split angle was 45° from the normal for each vessel arm. Low-cost epoxy adhesive resin is poured over the milled acrylic block and allowed to cure. The resulting resin mold was used to transfer the microchannel architecture onto a PDMS layer. Two equivalent PDMS layers were plasma bonded together to form a 3D vessel phantom. The phantom was placed at the iso-center of the MRI scanner with flow in the z direction with the vessel bifurcation in the horizontal (x)-plane to limit gravity based confounds. To help maximize bore size–no imaging coil was installed for targeting experiments. MAG suspensions (10 mL, 0.5 mg mL^{-1}) were flowed through the phantom entry point using a syringe pump at a flow rate of 0.5 mL min^{-1}. The output of each vessel was collected in an open Falcon tube for subsequent ICP-MS analysis for Fe content.

Magnetic resonance targeting followed Reigler et al. (2009).[27] For this, the gradients at 50% of G_{max} (330 mT m^{-1} — to avoid over heating), 2 ms on and 7 ms off, in the x-direction, until the suspension volume had been passed (≈20 min). Three experiments were completed. One with targeting in the +x direction (left hand vessel), one with targeting in the –x direction, and a control experiment with no magnetic targeting to account for natural flow discrepancies.

Endotoxin Removal: The removal of endotoxins from the MAG membrane involved incubating 20 µg of purified MAG with 1 mL of either 70% v/v ethanol, 1% v/v acetic acid, 0.25% v/v Triton X-100, 1% v/v Triton X-100, 0.25% v/v CHAPS, 1% v/v CHAPS or sterile PBS for 2 h on a tube rotator (50 rpm) at room temperature (RT). MAG (20 µg) suspended in 1 mL PBS were also autoclaved at 121 °C before treated MAG were placed on a neodymium magnet and washed three times with sterile PBS. Endotoxin concentrations were measured using the Limulus Amebocyte Lysate (LAL) Chromogenic Endpoint Assay (Hycult Biotech, UK). For this, samples were serially diluted (10^1–10^5) in endotoxin-free water and the assay performed following the manufacturer's protocol. Absorbance was read at 405 nm and endotoxin concentration per 50 µg of MAG calculated from the calibration curve.

Cell Viability: The effect of MAG on the viability of cell lines was assessed using the Alamar Blue Viability Assay (Sigma-Aldrich Ltd, UK). For this, cells were seeded into 96-well plates (1×10^5 cells per well) and incubated overnight prior to inoculation with 0.1 mg mL^{-1} solution of MAGs suspended in DMEM. Alamar Blue (10% v/v) was added to wells 5 days later for 2 h (37 °C, 5% v/v CO_2 humidified incubator). Fluorescence was read at excitation and emission wavelengths of 560 and 590 nm.

Flow Cytometry: Cellular uptake and cell viability experiments were performed in 12-well tissue culture plates (Costar, Corning Incorporated) at a seeding density of 2×10^5 cells per well. Cells were inoculated with DiD-labeled MAG, GFP-expressing OV and their complexes and analyzed by flow cytometry following trypsinization and the addition of TOPRO-3 viability dye (Thermo Fisher). Cellular uptake of MAG in the presence of a plate magnet (Thermo Fisher) was performed by adding 1, 3, and 10 µg of DiD-labeled MAG to pairs of 12-well plates ($n = 3$ per cell line). Plates were incubated for 0.5–1 h with one plate from each pair placed onto the plate magnet. Flow cytometry of trypsinized cells from all experiments were quantified using a BD LSRII flow cytometer (BD Biosciences) and FlowJo software following the recording of 10 000 events per sample.

Biochemical Analysis: Concentrations of secreted HMGB1 and ATP in the supernatant of infected and control cells were measured using commercially available ELISA kits [HMGB1 ELISA kit II (Shino-Test, Kanagawa, Japan) and ENLITEN ATP assay (Promega, Madison, WI)] according to the manufacturer's instructions.

Tumor Spheroids In Vitro: For tumor spheroid experiments, 96-well plates were coated with DMEM containing agarose prior to seeding with MDA-MB-231 cells at 2×10^4 cells per well. Following incubation for 5–7 days and an approximate cell density of 10^5 cells, spheroids were inoculated with HSV1716 or MAG-OV at an MOI of 10. Spheroid size was monitored by light microscopy (Leica DM1000) at x10 magnification. Flow cytometry as described above was used to assess cellular death 6 days postinfection.

Neutralizing Antibody: A sheep anti-HSV1 antiserum prepared by Virtuu Biologics Ltd was used to model the potential shielding properties of the MAG within the MAG-OV complex. For this, OV and MAG-OV samples at a concentration of $\approx 1 \times 10^7$ pfu were incubated with/without the antiserum for 18 h at 4 °C. These were then used to inoculate MDA-MB-231 cells for 24 h at 37 °C and cell viability quantified by flow cytometry, as described above.

In Vivo Studies: Animal procedures were carried out in accordance with the UK Animals (Scientific Procedures) Act 1986 with approval from the UK Home Office approval (PPL70/8670), the ARRIVE (Animal Research: Reporting of In Vivo Experiments) guidelines and the University of Sheffield Animal Welfare Ethical Review Body (AWERB). Female C57Bl/6 mice were obtained from Charles River Laboratory (Kent, UK) at 6–8 weeks and acclimatized in the Biological Services Laboratory for 7 days prior to experimentation. Animals were anesthetized using 3–4% v/v isofluorane in 70:30% v/v N_2O:O_2.

Magnetic Array: The magnetic device was designed using finite element method magnetics (FEMM). FEMM is a finite element solver for low frequency magnetics in the 2D plane and provides a way to model the magnetic field strength, measured in units of the Tesla (T). The configuration created used five single ($3 \times 3 \times 3$ mm^{-3}) magnets with fields pointing along different axes and the magnetic strength was maximized along the central plane of the magnet device. The configuration designed using FEMM was built using rare earth Neodymium Iron Boron (Nd-Fe-B)-grade N42 strength magnets (First4magnets.com). The size of each magnet was as in the model ($3 \times 3 \times 3$ mm^{-3}) and five individual magnets were glued together using Gorilla Glue Epoxy (www.gorillatough.com) to create the device. To determine how the magnetic field changed with distance and the force generated, a gaussmeter (GM 08, HIRST, Magnetic instruments Ltd) was used to measure the magnetic strength in Tesla. The strength of the magnet was 0.8 T.

Experimental Design: For tumor growth in female immunocompetent C57Bl/6 mice ($n = 8$ per group), 5×10^5 E0771-Luc cells were injected into the inguinal mammary fat pads in 50% matrigel:50% PBS. Mammary tumor growth was assessed by digital caliper measurement every 2–3 days and when tumors reached ≈150–200 mm^3, mice were randomly divided into groups and treatment initiated with groups receiving 3 intravenous (tail vein) 0.1 mL injections of PBS, MAG (0.002 µg mL^{-1}), OV (10^6 pfu mL^{-1}) or MAG-OV (0.002 µg mL+10^6 pfu mL^{-1}) with an interval of 5 days between (Figure 4a). A fifth group of mice received MAG-OV in the presence of an external magnetic array (0.7 T) secured to the tumor for 30 min, as described above. A survival study was performed whereby mice were culled and tissue harvested when primary tumors reached 1.5 cm^3 or mice lost ≥20% of their body weight. Tumor tissue was analyzed by NanoString and immunofluorescent detection of immune markers described below. Of note, animals were imaged once a week using luminescence in vivo imaging system

(IVIS Lumina II imaging, Caliper Life Sciences) following intraperitoneal injection of D-luciferin (150 mg kg^{-1}, Invitrogen). This was to track any metastatic burden.

Pharmacokinetic analysis of DiD-labeled MAG was investigated in tumor bearing FVB mice (n = 3 mice/group/timepoint) once PyMT-S1 tumors had reached a mean volume of 0.1 cm^3. Mice received a single 0.1 mL intravenous injection of MAG solution (0.1 mg mL) with or without 30 min magnetic targeting, as described above. Mice were sacrificed 1, 4, 8, and 24 h postinjection. Approximately 1 mL of blood was collected by cardiac puncture using sodium heparin as an anticoagulant. Red blood cells were lysed and DiD-labeled MAG quantified by flow cytometry using the BD LSRII flow cytometer. Tumor was collected from each mouse and snap frozen prior to cell dissociation and flow cytometric determination of DiD-labeled MAG per mg of tissue.

Immunofluorescence Staining: Immunofluorescence of tumors was carried out on 4 µm tumor cryosections. Sections were blocked with 1% w/v BSA and 5% v/v goat serum for 30 min and incubated, at room temperature, with primary conjugated antibodies against CRT (505 207, 1:100 dilution, BioLegend, San Diego, CA), CD3 (20-0031, 1:200 dilution, BD Pharmingen, Franklin Lakes, NJ), CD31 (102 515, 1:100 dilution, BioLegend), CD4 (100 425, 1:50 dilution, BioLegend), CD8 (100 707, 1:100 dilution, BioLegend), F4/80 (MCA497A488, 1:25 dilution, AbD Serotec, Oxford, UK), GFP (ab290, 1:1000 dilution, Abcam, Cambridge, UK), IFN-γ(505 809, 1:100 dilution, BioLegend), NK-1.1 (108 723, 1:100 dilution, BioLegend), and PD1 (135 215, 1:100 dilution, BioLegend). After 1-h, sections were counterstained with 50 ng mL^{-1} DAPI solution and mounted with ProLong Antifade (Thermo Fisher Scientific). Images were captured using a Nikon A1 confocal microscope at x40 magnification. Formalin-fixed, paraffin-embedded tissues were rehydrated, peroxidase blocked, antigen retrieved, serum blocked, and then incubated with primary antibodies for 1–2 h. Primary antibodies were detected with ABC or Polymer detection kits followed by chromogen staining with 3′-Diaminobenzidine (DAB). Following Hematoxylin and Eosin staining, slides were visualized using the Hamamatsu NanoZoomer XR scanner (Hamamatsu, Hertfordshire, UK). Positive cells were quantified using ImageScope (Leica Biosystems) and expressed relative to the total number of cells in the field of view from 5 randomly selected areas per tumor.

Real Time PCR: Total RNA was extracted using Qiagen RNeasy Mini Kit (Qiagen) before being reverse transcribed into cDNA using High-capacity RNA-to cDNA Kit (Thermo Fisher Scientific). Relative mRNA expression was compared with the housekeeping gene GAPDH and assessed using an ABI 7900 PCR System (Perkin Elmer) and SYBR Green PCR Master Mix (all reagents were purchased from Applied Biosystems via Thermo Fisher Scientific). Fold change in gene expression between treatment groups was analyzed by inserting C_t values into Data Assist V3.01 software (Applied Biosystems) and changes in gene expression were only analyzed for genes with a C_t value of ≤25.

NanoString nCounter Gene Expression Analysis: Amplification-free gene expression profiling of tumor tissue using a NanoString nCounter FLEX platform and the nCounter PanCancer Immune Profiling Panel, which consist of 750 immune related genes and 20 housekeeping genes (NanoString Technologies Inc.) was undertaken in the John van Geest Cancer Research Centre (Nottingham Trent University). For this, total mRNA was extracted from cultured MDMs or murine tissues using the RNeasy Mini Kit (Qiagen) and quality controlled using a NanoDrop 8000 Spectrophotometer. For gene expression profiling, 150 ng of total RNA from each sample was used for NanoString probe hybridization which was undertaken overnight (20 h) at 65 °C in a PCR machine with heated lid (each reaction mixture contains 5 µL of RNA solution (150 ng), 8 µL of reporter probe and 2 µL of capture probe). After overnight hybridization, excess probes were removed using the NanoString nCounter Prep Station and magnetic beads, hybridized mRNA/probe were immobilized on a streptavidin-coated cartridge. The processed cartridge was subsequently scanned, and raw data generated at high-resolution (555 fields of view, fov) using a NanoString nCounter digital analyzer platform and processed using nSolver Data Analysis Software (V.4.0). Imaging quality control (QC), mRNA positive control QC, and normalization QC were checked, and all the samples were with the quality parameters of NanoString gene expression assays. Differential expression, pathway and cell type scoring was performed using the nSolver Advanced Analysis Module v.2.0.115. Data normalization was performed using the geNorm algorithm for the selection of the best housekeeping genes. Genes which showed ≥ 2, fold change in their expression with a BY (Benjamini-Yekutieli procedure) p value ≤ 0.05 were considered significantly different between the groups.

Flow Cytometric Analysis: In brief, tumors were dispersed by enzymatic digestion after first dicing into pieces ≈1 mm^3. Tumor pieces were incubated for 40 min at 37 °C in serum-free IMDM (VWR International, PA) supplemented with 2 mg mL^{-1} dispase, 0.2 mg mL^{-1} collagenase IV (Sigma-Aldrich, St. Louis, MO), and 100 U mL^{-1} DNase (Merck Millipore, Burlington, MA). Dispersed tumors were passed through 70 µm nylon filters (Becton Dickinson, Franklin Lakes, NJ) and maintained on ice in PBS or cryo-preserved in 90% v/v FBS and 10% v/v DMSO for flow cytometric analysis.

The mouse immune cell populations analyzed were as follows: Neutrophils ($CD45^+CD11b^+Ly6G^+$), Monocytes ($CD45^+CD11b^+Ly6G^{neg}Ly6C^+F4/80^{Lo}$), Macrophages ($CD45^+CD11b^+Ly6G^{neg}Ly6C^{Lo}F4/80^{Hi}$), T_{Helper} ($CD45^+CD3^+CD4^+$), and Cytotoxic T-cells ($CD45^+CD3^+CD8^+$). The membrane impermeant, fixable, amine reactive dye Zombie UV Fixable (BioLegend Inc., San Diego, CA) was used to discriminate between live and dead cells. All data are presented as proportion of viable leukocytes.

Statistical Analysis: Group-wise comparisons were carried out using one-way independent ANOVA with Tukey multiple comparison test (unless otherwise stated in the figure legends) using GraphPad Prism software version 7.0. Statistical significance was defined as $p \leq 0.05$.

Supporting Information

Supporting Information is available from the Wiley Online Library or from the author.

Acknowledgements

Financial support provided by Cancer Research UK (CRUK grant reference: C25574/A24321), EPSRC for the Kratos LiPPS XPS instrument grant (EP/K005138/1), and the European Union's Horizon 2020 research and innovation programme under the Marie Sklodowska Curie grant agreement No 777682 (CANCER). HSV1716 was kindly provided by Virtuu Biologics Ltd. Special thanks to Dario Carugo, University of Southampton for providing the phantom and Devashish Das for the initial MR imaging.

Conflict of Interest

The authors declare no conflict of interest.

Author Contributions

F.H.N.H. and H.A.-J. contributed equally to this work. M.M. initiated this project. F.H.N.H., H.A.-J., S.S., and J.C. synthesized the materials. F.H.N.H. and H.A.-J. performed the experiments. F.H.N.H. analyzed the data. P.P. designed the magnetic array for local magnetic targeting. C.C.R. performed endotoxin removal and quantification. J.V. and A.G.P. performed Nanostring nCounter gene profiling and associated data analysis and interpretation. E.S. performed the XPS experimentation. D.A.A. and J.F.N. performed the VSM modelling. A.J.K. completed in vivo and in vitro MRI measures and analysis. F.H.N.H. wrote the manuscript with important contributions from all authors. All authors have given approval to the final version of the manuscript.

Data Availability Statement

The data that support the findings of this study are available from the corresponding author upon reasonable request.

Keywords

breast cancer, magnetosomes, magnetic targeting, nanomedicine, nanoparticles, oncolytic virotherapy

Received: August 9, 2021
Revised: December 18, 2021
Published online:

[1] D. B. Johnson, I. Puzanov, M. C. Kelley, *Immunotherapy* **2015**, *7*, 611.
[2] I. R. Eissa, I. Bustos-Villalobos, T. Ichinose, S. Matsumura, Y. Naoe, N. Miyajima, D. Morimoto, N. Mukoyama, W. Zhiwen, M. Tanaka, H. Hasegawa, S. Sumigama, B. Aleksic, Y. Kodera, H. Kasuya, *Cancers* **2018**, *10*, 356.
[3] L. Li, S. Liu, D. Han, B. Tang, J. Ma, *Front Oncol.* **2020**, *10*, 475.
[4] A. M. Noonan, M. R. Farren, S. M. Geyer, Y. Huang, S. Tahiri, D. Ahn, S. Mikhail, K. K. Ciombor, S. Pant, S. Aparo, J. Sexton, J. L. Marshall, T. A. Mace, C. S. Wu, B. El-Rayes, C. D. Timmers, J. Zwiebel, G. B. Lesinski, M. A. Villalona-Calero, T. S. Bekaii-Saab, *Mol. Ther.* **2016**, *24*, 1150.
[5] S. R. Jhawar, A. Thandoni, P. K. Bommareddy, S. Hassan, F. J. Kohlhapp, S. Goyal, J. M. Schenkel, A. W. Silk, A. Zloza, *Front Oncol.* **2017**, *7*, 202.
[6] F. Howard, M. Muthana, *Nanomedicine* **2020**, *15*, 93.
[7] M. S. Ferguson, N. R. Lemoine, Y. Wang, *Adv. Virol.* **2012**, *2012*, 805629.
[8] J. Wojton, B. Kaur, *Cytokine Growth Factor Rev.* **2010**, *21*, 127.
[9] C. J. Breitbach, J. Burke, D. Jonker, J. Stephenson, A. R. Haas, L. Q. Chow, J. Nieva, T. H. Hwang, A. Moon, R. Patt, A. Pelusio, F. Le Boeuf, J. Burns, L. Evgin, N. De Silva, S. Cvancic, T. Robertson, J. E. Je, Y. S. Lee, K. Parato, J. S. Diallo, A. Fenster, M. Daneshmand, J. C. Bell, D. H. Kirn, *Nature* **2011**, *477*, 99.
[10] M. Muthana, A. Giannoudis, S. D. Scott, H. Y. Fang, S. B. Coffelt, F. J. Morrow, C. Murdoch, J. Burton, N. Cross, B. Burke, R. Mistry, F. Hamdy, N. J. Brown, L. Georgopoulos, P. Hoskin, M. Essand, C. E. Lewis, N. J. Maitland, *Cancer Res.* **2011**, *71*, 1805.
[11] Y. Wang, H. Huang, H. Zou, X. Tian, J. Hu, P. Qiu, H. Hu, G. Yan, *Mol. Pharm.* **2019**, *16*, 779.
[12] G. K. Grunwald, A. Vetter, K. Klutz, M. J. Willhauck, N. Schwenk, R. Senekowitsch-Schmidtke, M. Schwaiger, C. Zach, E. Wagner, B. Goke, P. S. Holm, M. Ogris, C. Spitzweg, *Mol. Ther. Nucl. Acids* **2013**, *2*, e131.
[13] N. Francini, D. Cochrane, S. Illingworth, L. Purdie, G. Mantovani, K. Fisher, L. W. Seymour, S. G. Spain, C. Alexander, *Bioconjug. Chem.* **2019**, *30*, 1244.
[14] A. Iscaro, N. F. Howard, M. Muthana, *Curr. Pharm. Des.* **2019**, *25*, 1962.
[15] S. Staniland, W. Williams, N. Telling, G. Van Der Laan, A. Harrison, B. Ward, *Nat. Nanotechnol.* **2008**, *3*, 158.
[16] M. Hanson, *J. Magnet. Matgnet. Mater.* **1991**, *96*, 105.
[17] X. Wang, P. J. Quinn, *Subcell Biochem.* **2010**, *53*, 3.
[18] R. L.e Fevre, M. Durand-Dubief, I. Chebbi, C. Mandawala, F. Lagroix, J. P. Valet, A. Idbaih, C. Adam, J. Y. Delattre, C. Schmitt, C. Maake, F. Guyot, E. Alphandery, *Theranostics* **2017**, *7*, 4618.
[19] Y. Hamdous, I. Chebbi, C. Mandawala, R. L.e Fevre, F. Guyot, O. Seksek, E. Alphandery, *J. Nanobiotechnol.* **2017**, *15*, 74.
[20] S. Han, C. Wang, X. Qin, J. Xia, A. Wu, *J. Exp. Clin. Cancer Res.* **2017**, *36*, 83.
[21] H. Prakash, V. Nadella, S. Singh, H. Schmitz-Winnenthal, *Sci. Rep.* **2016**, *6*, 31490.
[22] S. Jain, P. Dash, A. P. Minz, S. Satpathi, A. G. Samal, P. K. Behera, P. S. Satpathi, S. Senapati, *Prostate* **2019**, *79*, 168.
[23] S. Li, X. Xu, M. Jiang, Y. Bi, J. Xu, M. Han, *Mol. Med. Rep.* **2015**, *11*, 4454.
[24] S. Meriaux, M. Boucher, B. Marty, Y. Lalatonne, S. Preveral, L. Motte, C. T. Lefevre, F. Geffroy, F. Lethimonnier, M. Pean, D. Garcia, G. Adryanczyk-Perrier, D. Pignol, N. Ginet, *Adv. Healthcare Mater.* **2015**, *4*, 1076.
[25] M. Mahmoudi, A. Tachibana, A. B. Goldstone, Y. J. Woo, P. Chakraborty, K. R. Lee, C. S. Foote, S. Piecewicz, J. C. Barrozo, A. Wakeel, B. W. Rice, C. B. BellIii, P. C. Yang, *Sci. Rep.* **2016**, *6*, 26960.
[26] S. Mannucci, S. Tambalo, G. Conti, L. Ghin, A. Milanese, A. Carboncino, E. Nicolato, M. R. Marinozzi, D. Benati, R. Bassi, P. Marzola, A. Sbarbati, *Contrast Media Mol. Imaging* **2018**, *2018*, 2198703.
[27] J. Riegler, J. A. Wells, P. G. Kyrtatos, A. N. Price, Q. A. Pankhurst, M. F. Lythgoe, *Biomaterials* **2010**, *31*, 5366.
[28] M. Muthana, A. J. Kennerley, R. Hughes, E. Fagnano, J. Richardson, M. Paul, C. Murdoch, F. Wright, C. Payne, M. F. Lythgoe, N. Farrow, J. Dobson, J. Conner, J. M. Wild, C. Lewis, *Nat. Commun.* **2015**, *6*, 8009.
[29] N. Gal, S. Massalha, O. Samuelly-Nafta, D. Weihs, *Med. Eng. Phys.* **2015**, *37*, 478.
[30] N. L. Chaves, I. Estrela-Lopis, J. Bottner, C. A. Lopes, B. C. Guido, A. R. de Sousa, S. N. Bao, *Int. J. Nanomed.* **2017**, *12*, 5511.
[31] M. M. Yallapu, S. F. Othman, E. T. Curtis, B. K. Gupta, M. Jaggi, S. C. Chauhan, *Biomaterials* **2011**, *32*, 1890.
[32] E. W. Thompson, S. Paik, N. Brünner, C. L. Sommers, G. Zugmaier, R. Clarke, T. B. Shima, J. Torri, S. Donahue, M. E. Lippman, G. R. Martin, R. B. Dickson, *J. Cell. Physiol.* **1992**, *150*, 534.
[33] N. Sun, H. N. Xu, Q. Luo, L. Z. Li, *Adv. Exp. Med. Biol.* **2016**, *923*, 121.
[34] I. Mellman, Y. Yarden, *Cold Spring Harb. Perspect. Biol.* **2013**, *5*, a016949.
[35] O. Kepp, L. Senovilla, I. Vitale, E. Vacchelli, S. Adjemian, P. Agostinis, L. Apetoh, F. Aranda, V. Barnaba, N. Bloy, L. Bracci, K. Breckpot, D. Brough, A. Buqué, M. G. Castro, M. Cirone, M. I. Colombo, I. Cremer, S. Demaria, L. Dini, A. G. Eliopoulos, A. Faggioni, S. C. Formenti, J. Fučíková, L. Gabriele, U. S. Gaipl, J. Galon, A. Garg, F. Ghiringhelli, N. A. Giese, et al., *OncoImmunology* **2014**, *3*, e955691.
[36] L. I. Gold, P. Eggleton, M. T. Sweetwyne, L. B. Van Duyn, M. R. Greives, S. M. Naylor, M. Michalak, J. E. Murphy-Ullrich, *FASEB J.* **2010**, *24*, 665.
[37] L. Zhang, M. B. Steele, N. Jenks, J. Grell, M. Behrens, R. Nace, S. Naik, M. J. Federspiel, S. J. Russell, K. W. Peng, *Mol. Ther.* **2016**, *24*, 2109.
[38] H. Maeda, *Proc. Jpn. Acad. Ser. B: Phys. Biol. Sci.* **2012**, *88*, 53.
[39] Y. Nakamura, A. Mochida, P. L. Choyke, H. Kobayashi, *Bioconjug. Chem.* **2016**, *27*, 2225.
[40] F. Scherer, M. Anton, U. Schillinger, J. Henke, C. Bergemann, A. Kruger, B. Gansbacher, C. Plank, *Gene Ther.* **2002**, *9*, 102.
[41] N. Tresilwised, P. Pithayanukul, O. Mykhaylyk, P. S. Holm, R. Holzmuller, M. Anton, S. Thalhammer, D. Adiguzel, M. Doblinger, C. Plank, *Mol. Pharm.* **2010**, *7*, 1069.
[42] W. Huang da, B. T. Sherman, R. A. Lempicki, *Nat. Protoc.* **2009**, *4*, 44.
[43] J. C. Hu, R. S. Coffin, C. J. Davis, N. J. Graham, N. Groves, P. J. Guest, K. J. Harrington, N. D. James, C. A. Love, I. McNeish,

L. C. Medley, A. Michael, C. M. Nutting, H. S. Pandha, C. A. Shorrock, J. Simpson, J. Steiner, N. M. Steven, D. Wright, R. C. Coombes, *Clin. Cancer Res.* **2006**, *12*, 6737.
[44] M. C. Brown, E. K. Holl, D. Boczkowski, E. Dobrikova, M. Mosaheb, V. Chandramohan, D. D. Bigner, M. Gromeier, S. K. Nair, *Sci. Transl. Med.* **2017**, *9*, http://dx.doi.org/10.1126/scitranslmed.aan4220.
[45] A. Melcher, *Mol. Ther.* **2018**, *26*, 1875.
[46] H. H. Soliman, H. S. Han, D. Hogue, B. Mooney, R. L. Costa, M. C. Lee, B. Niell, A. Williams, A. Chau, S. Falcon, N. Khakpour, A. Soyano, A. J. Armaghani, R. J. Weinfurtner, S. Hoover, J. Kiluk, M. Rosa, B. Fridley, H. T. Khong, B. J. Czerniecki, *J. Clin. Oncol.* **2021**, *39*, 578.
[47] R. Nanda, L. Q. Chow, E. C. Dees, R. Berger, S. Gupta, R. Geva, L. Pusztai, K. Pathiraja, G. Aktan, J. D. Cheng, V. Karantza, L. Buisseret, *J. Clin. Oncol.* **2016**, *34*, 2460.
[48] J. Conner, L. Braidwood, S. M. Brown, *Gene Ther.* **2008**, *15*, 1579.
[49] D. Carugo, J. Y. Lee, A. Pora, R. J. Browning, L. Capretto, C. Nastruzzi, E. Stride, *Biomed. Microdevices* **2016**, *18*, 4.